


RESEARCH ARTICLE | OCTOBER 20 2022

Revisit of the oblique-breakdown regime in supersonic boundary layers and mechanism of the extra amplification of streak modes

Runjie Song; Ming Dong  ; Lei Zhao 



Physics of Fluids 34, 104110 (2022)

<https://doi.org/10.1063/5.0117622>



View
Online



Export
Citation

CrossMark

Articles You May Be Interested In

Two routes to the one-dimensional discrete nonpolynomial Schrödinger equation

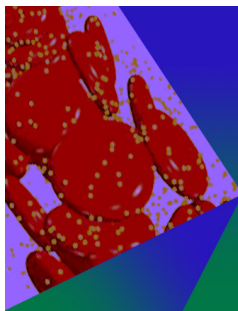
Chaos (October 2009)

Secondary instability of the hypersonic high-enthalpy boundary layers with thermal–chemical nonequilibrium effects

Physics of Fluids (March 2021)

Nonlinear interaction between two second-mode disturbances with the same frequency in a hypersonic boundary layer over a swept blunt plate

Physics of Fluids (April 2021)



Physics of Fluids

Special Topic: Flow and Forensics

Submit Today!

 AIP
Publishing

 AIP
Publishing

Revisit of the oblique-breakdown regime in supersonic boundary layers and mechanism of the extra amplification of streak modes

Cite as: Phys. Fluids **34**, 104110 (2022); doi: 10.1063/5.0117622
Submitted: 1 August 2022 · Accepted: 18 September 2022 ·
Published Online: 20 October 2022




View Online



Export Citation



CrossMark

Runjie Song,¹ Ming Dong,^{1,2,a)}  and Lei Zhao^{3,a)} 

AFFILIATIONS

¹State Key laboratory of Nonlinear Mechanics, Institute of Mechanics, Chinese Academy of Sciences, Beijing 100190, China

²Sino-Russian Mathematics Center, Peking University, Beijing 100871, China

³Department of Mechanics, Tianjin University, Tianjin, 300072, China

^{a)}Authors to whom correspondence should be addressed: dongming@imech.ac.cn and lei_zhao@tju.edu.cn

ABSTRACT

In the low-Mach-number supersonic boundary layers, the oblique-breakdown regime may be the most efficient route to trigger the laminar-turbulent transition, because the most unstable Mack first mode always appears as an oblique wave. In this paper, we revisit this issue by use of the nonlinear parabolized stability equation (NPSE) approach and particularly focus on the extra amplification of the streak mode generated by the direct interaction of the introduced oblique modes. This mechanism is then well explained based on the weakly nonlinear analysis, and its predictions on the evolution of the streak mode and the two-dimensional traveling-wave mode are quantitatively confirmed by the NPSE calculations. Additionally, the important role of the streak mode, leading to the secondary instability, on triggering the transition onset is identified.

Published under an exclusive license by AIP Publishing. <https://doi.org/10.1063/5.0117622>

I. INTRODUCTION

Laminar-turbulent transition in supersonic boundary layers is always an attractive issue of practical importance in recent decades due to its relevance to the aerodynamic design of high-speed vehicles.^{1,2} In a low-perturbation environment, boundary-layer transition follows a natural route,³ in which four phases, that is, the receptivity, linear instability, nonlinear breakdown, and turbulence, appear in sequence. In the pioneering work of the linear stability analysis of supersonic boundary layers, Mack⁴ reported that more than one discrete-mode solutions exist, which are named as the Mack first, second, . . . , modes according to the ascending order of their frequency. The linear evolution of these modes was confirmed by a great number of subsequent numerical works, such as Refs. 1 and 2. It was revealed by the asymptotic analysis that only the first Mack mode with $\Theta > \tan^{-1}\sqrt{M^2 - 1}$ (where Θ and M denote the wave angle and Mach number, respectively) belongs to the viscous nature,^{5,6} while the quasi-two-dimensional first and all the higher-order Mack modes are inviscid.⁷⁻⁹ When the unstable modes are accumulated to finite amplitudes, the nonlinear interaction among different Fourier components becomes the leading-order impact, which includes the oblique-mode breakdown,¹⁰⁻¹⁵ the fundamental resonance,^{16,17} and subharmonic resonance.¹⁸

The oblique-mode breakdown regime was first identified by Thumm¹⁰ and Fasel *et al.*,¹¹ based on the direct numerical simulation (DNS) of a Mach 1.6 flat-plate boundary layer. It was found that a pair of finite-amplitude oblique waves with the same frequency but opposite spanwise wavenumbers form a stationary streak mode due to the triadic resonance. The introduced oblique waves show almost linear growth for the majority of the laminar phase, while the streak mode grows with a greater rate and overwhelms the former modes in a short distance before the breakdown of the laminar flow. After the streak mode becoming dominant, the higher-order harmonic modes and the mean-flow distortion grow more rapidly, which eventually leads to the transition to turbulence. A subsequent study using the nonlinear parabolic stability equations (NPSE) approach by Chang and Malik¹² also confirmed this scenario. It was also reported that for low-Mach-number supersonic boundary layers, the oblique-mode breakdown regime is more efficient on triggering transition than the fundamental and subharmonic resonance regimes because the most unstable Mack first modes are always oblique.

In an early experimental study, Ermolaev *et al.*¹⁹ reported an “asymmetric subharmonic resonance” in a Mach 2 supersonic boundary layer, in which the dominant perturbations consist of both the

fundamental oblique waves and subharmonic oblique waves. A subsequent DNS study¹⁴ revisited the same configuration and showed that the fundamental perturbations themselves can lead to oblique-mode breakdown. Considering the expensive computational load of DNS, the NPSE approach is more preferred and its accuracy was confirmed by Mayer *et al.*²⁰ The oblique-breakdown regime also exists in incompressible boundary layers²¹ and hypersonic boundary layers.²² Particularly, in a Mach 6 flat-plate boundary layer, Franko *et al.*²² further reported an overshoot of the skin friction and heat flux during the transition process due to the generation of the streamwise vortices by the oblique-wave interaction. Actually, the oblique-mode breakdown regime can be observed in more generic configurations, such as the generation of longitudinal streaks from the development of a wave packet.²³

Although the phenomenon of the oblique-mode breakdown has been extensively studied for decades, theoretical works explaining its inherent mechanisms are less sufficient. A decent asymptotic analysis of the oblique-mode breakdown regime in supersonic boundary layers was presented by Leib and Lee.¹³ Employing the nonlinear-critical-layer theory as in Refs. 24 and 25, they derived the perturbation evolution by solving the amplitude equation. Their results showed that the most rapidly growing oblique waves are enhanced by the nonlinear critical layer and the amplitude ends in a singularity at a finite downstream position, leading to the breakdown of the laminar flow. However, the numerical results^{10,11} indicate that the stationary streak mode could be extra amplified before the oblique modes reaching the nonlinear phase or reaching the vicinity of the upper-branch neutral point. This phenomenon still remains puzzling to us, which is the main task of the present work.

The rest of this paper is structured as follows. In Sec. II, we introduce the physical model and the governing equations. The numerical results of the oblique-mode breakdown process obtained by the NPSE approach will be presented in Sec. III. In Sec. IV, a weakly nonlinear analysis is presented to explain the extra amplification of the streak mode theoretically, and its prediction will be compared with the NPSE results. In Sec. V, we will show the effect of the streak mode on the growth of other harmonic modes and its role on transition. Finally, we conclude our numerical observations and present remarks and discussions in Sec. VI.

II. MATHEMATICAL DETAILS

A. Physical model and governing equations

For a demonstration of the oblique-breakdown regime, we choose the physical model to be studied as a supersonic boundary layer over a sharp cone that is inserted into a supersonic stream with zero angle of attack, as shown in Fig. 1. The half-apex angle of the cone θ is small, and a viscous boundary layer is formed behind the cone-shaped shock. The body-fitted coordinate system (x^*, y^*, φ) is employed with its origin locating at the cone tip, where x^* and y^* are along and perpendicular to the wall, respectively, and φ is the circumferential angle. Throughout this paper, the superscript $*$ and subscript e denote the dimensional and the boundary-layer edge quantities, respectively. At a location $x^* = x_0^*$, a pair of oblique instability modes is introduced and their nonlinear evolution will be calculated by NPSE. The computation domain is shown by the blue box in Fig. 1.

The velocity field $\mathbf{u}=(u, v, w)$, density ρ , temperature T , pressure p , and dynamic viscosity μ are normalized by U_e^* , ρ_e^* , T_e^* , $\rho_e^* U_e^{*2}$, and μ_e^* ,

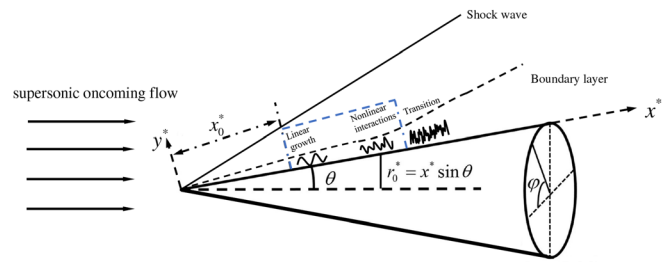


FIG. 1. Sketch of the physical model.

respectively, where U_e^* , T_e^* , and ρ_e^* are the velocity, temperature, and density at the boundary-layer edge. The unit length is taken to be the characteristic length of the boundary layer at the entrance of the computation domain, $\delta^* = \sqrt{\frac{x_0^* \mu_e^*}{\rho_e^* U_e^*}}$. Thus, the coordinate system and time are normalized as $(x, y) = (x^*, y^*)/\delta^*$ and $t = t^* \delta^*/U_e^*$, respectively. The flow system is governed by the characteristic parameters, the Reynolds number $R = \rho_e^* U_e^* \delta^*/\mu_e^*$ and the Mach number $M = U_e^*/a_e^*$, where a_e^* is the sound speed at the edge of the boundary layer.

The dimensionless compressible Navier–Stokes (N–S) equations are

$$\begin{aligned} \frac{D\rho}{Dt} &= -\rho \nabla \cdot \mathbf{u}, \\ \rho \frac{D\mathbf{u}}{Dt} &= -\frac{\nabla(\rho T)}{\gamma M^2} + \frac{1}{R} \left[2\nabla \cdot (\mu \mathbf{S}) - \frac{2}{3} \nabla(\mu \nabla \cdot \mathbf{u}) \right], \\ \frac{1}{\gamma} \rho \frac{DT}{Dt} &= \frac{\gamma-1}{\gamma} T \frac{D\rho}{Dt} + \frac{(\gamma-1)M^2}{R} \left[2\mu \mathbf{S} : \mathbf{S} - \frac{2}{3} \mu (\nabla \cdot \mathbf{u})^2 \right] \\ &\quad + \frac{1}{PrR} \nabla \cdot (\mu \nabla T), \end{aligned} \quad (1)$$

where $\mathbf{S} = [\nabla \mathbf{u} + (\nabla \mathbf{u})^T]/2$ is the rate of strain tensor, Pr is the Prandtl number, γ is the ratio of specific heat, $\frac{D}{Dt} = \frac{\partial}{\partial t} + \mathbf{u} \cdot \nabla$ denotes the material derivative, and “ \cdot ” denotes the double-dot product of two second-order tensors. The equation of the state, $p = \frac{\rho T}{\gamma M^2}$, has been used to eliminate the pressure p in the momentum equations. Sutherland’s viscosity law is assumed, namely, $\mu(T) = (1+C)T^{3/2}/(T+C)$ with $C = 110.4/T_e^*$. In addition, the distance to the cone axis r can be defined as

$$r = r_0 + y \cos \theta, \quad (2)$$

with $r_0 = x \sin \theta$ denoting the radius on the wall. The instantaneous flow field $\phi \equiv (\rho, u, v, w, T)$ can be decomposed into a steady base flow $\Phi_B \equiv (\rho_B, U_B, R^{-1} V_B, 0, T_B)$ and an unsteady perturbation $\tilde{\phi}$,

$$\phi = \Phi_B(x, y) + \tilde{\phi}(x, y, \varphi, t). \quad (3)$$

B. Base flow

Because the base flow varies slowly with x , we introduce a slow variable

$$X = R^{-1}x, \quad (4)$$

such that $\partial_X \Phi_B = O(1)$. Considering that the base flow is steady and invariant with φ , the N–S system (1) is reduced to

$$\begin{aligned} \frac{\partial(\rho_B U_B \bar{r})}{\partial X} + \frac{\partial(\rho_B V_B \bar{r})}{\partial y} &= 0, \\ \rho_B \left[U_B \frac{\partial U_B}{\partial X} + V_B \frac{\partial U_B}{\partial y} \right] &= \frac{\partial}{\partial y} \left(\mu_B \frac{\partial U_B}{\partial y} \right), \\ \rho_B \left(U_B \frac{\partial T_B}{\partial X} + V_B \frac{\partial T_B}{\partial y} \right) &= (\gamma - 1) M^2 \mu_B \left(\frac{\partial U_B}{\partial y} \right)^2 \\ &+ \frac{1}{Pr} \left[\frac{\partial}{\partial y} \left(\mu_B \frac{\partial T_B}{\partial y} \right) \right], \\ \rho_B T_B &= 1, \end{aligned} \tag{5}$$

where $\bar{r} = X \sin \theta$, and the $O(R^{-1})$ terms are neglected. The pressure gradient is secondary from the potential-flow analysis. The no-slip, non-penetration, and isothermal boundary conditions are applied at the wall

$$(U_B, V_B, T_B) = (0, 0, T_w) \quad \text{at } y = 0, \tag{6}$$

where T_w is the dimensionless wall temperature. Note that for an adiabatic wall, we simply change the wall temperature condition to $\partial T_B / \partial y = 0$. The upper boundary conditions read

$$(\rho_B, U_B, T_B) \rightarrow (1, 1, 1) \quad \text{as } y \rightarrow \infty. \tag{7}$$

Introducing the Mangler transformation,²⁶

$$\begin{aligned} \tilde{X} &= \int_0^X \bar{r}^2 d\hat{X} = \frac{1}{3} X^3 \sin^2 \theta, \quad \tilde{y} = \bar{r} y = X \sin \theta y, \\ \tilde{V}_B &= \frac{1}{\bar{r}} \left(V_B + \frac{1}{\bar{r}} \frac{d\bar{r}}{dX} y U_B \right) = \frac{1}{X \sin \theta} \left(V_B + \frac{y}{X} U_B \right), \end{aligned} \tag{8}$$

the system (5) can be regularized into a planar form

$$\begin{aligned} \frac{\partial(\rho_B U_B)}{\partial \tilde{X}} + \frac{\partial(\rho_B \tilde{V}_B)}{\partial \tilde{y}} &= 0, \\ \rho_B \left[U_B \frac{\partial U_B}{\partial \tilde{X}} + \tilde{V}_B \frac{\partial U_B}{\partial \tilde{y}} \right] &= \frac{\partial}{\partial \tilde{y}} \left(\mu_B \frac{\partial U_B}{\partial \tilde{y}} \right), \\ \rho_B \left(U_B \frac{\partial T_B}{\partial \tilde{X}} + \tilde{V}_B \frac{\partial T_B}{\partial \tilde{y}} \right) &= (\gamma - 1) M^2 \mu_B \left(\frac{\partial U_B}{\partial \tilde{y}} \right)^2 \\ &+ \frac{1}{Pr} \left[\frac{\partial}{\partial \tilde{y}} \left(\mu_B \frac{\partial T_B}{\partial \tilde{y}} \right) \right], \\ \rho_B T_B &= 1. \end{aligned} \tag{9}$$

System (9) is the same as the compressible Blasius similarity solution for a flat plate, which can be found in Refs. 12, 16, 27, and 28.

C. Perturbations

Substituting the decomposition (3) into the Navier–Stokes equation (1), and subtracting the base flow out, we obtain the nonlinear disturbance equations

$$\begin{aligned} \Gamma \frac{\partial \tilde{\phi}}{\partial t} + \mathbf{A} \frac{\partial \tilde{\phi}}{\partial x} + \mathbf{B} \frac{\partial \tilde{\phi}}{\partial y} + \mathbf{C} \frac{\partial \tilde{\phi}}{\partial \varphi} + \mathbf{D} \tilde{\phi} + \mathbf{V}_{xx} \frac{\partial^2 \tilde{\phi}}{\partial x^2} + \mathbf{V}_{yy} \frac{\partial^2 \tilde{\phi}}{\partial y^2} \\ + \mathbf{V}_{\varphi\varphi} \frac{\partial^2 \tilde{\phi}}{\partial \varphi^2} + \mathbf{V}_{xy} \frac{\partial^2 \tilde{\phi}}{\partial x \partial y} + \mathbf{V}_{x\varphi} \frac{\partial^2 \tilde{\phi}}{\partial x \partial \varphi} + \mathbf{V}_{y\varphi} \frac{\partial^2 \tilde{\phi}}{\partial y \partial \varphi} = \mathbf{F}, \end{aligned} \tag{10}$$

where the coefficient matrices $\Gamma, \mathbf{A}, \mathbf{B}, \mathbf{C}, \mathbf{D}, \mathbf{V}_{xx}, \mathbf{V}_{yy}, \mathbf{V}_{\varphi\varphi}, \mathbf{V}_{xy}, \mathbf{V}_{y\varphi}$, and $\mathbf{V}_{x\varphi}$ are functions of the base flow quantities and \mathbf{F} is a vector corresponding to the nonlinear terms. They can be found in Appendix A.

1. Linear instability analysis

Under the parallel-flow assumption, the perturbation $\tilde{\phi}$ is expressed in terms of a traveling-wave form

$$\tilde{\phi} = \varepsilon \hat{\phi}(y) \exp[i(\alpha x + n\varphi - \omega t)] + \text{c.c.}, \tag{11}$$

where α, n , and ω represent the streamwise wavenumber, circumferential wavenumber, and frequency, c.c represents the complex conjugation, and $i \equiv \sqrt{-1}$ and $\hat{\phi}$ denote the normalized shape function. In what follows, the shape functions are normalized by the maximum norm with the streamwise velocity perturbation. $\varepsilon \ll 1$ measures the amplitude of the perturbation. We are interested in the spatial mode for which only $\alpha = \alpha_r + i\alpha_i$ is complex with $-\alpha_i$ representing its growth rate. Substituting (11) into (10) and retaining the $O(\varepsilon)$ terms, we arrive at compressible Orr–Sommerfeld (O–S) equation

$$\tilde{\mathbf{B}} \frac{\partial \hat{\phi}}{\partial y} + \mathbf{V}_{yy} \frac{\partial^2 \hat{\phi}}{\partial y^2} + \tilde{\mathbf{D}} \hat{\phi} = 0, \tag{12}$$

where

$$\begin{aligned} \tilde{\mathbf{B}} &= \mathbf{B} - i\alpha \mathbf{V}_{xy} - in \mathbf{V}_{y\varphi}, \\ \tilde{\mathbf{D}} &= -i\omega \Gamma + i\alpha \mathbf{A} + in \mathbf{C} + \mathbf{D} + \alpha^2 \mathbf{V}_{xx} + n^2 \mathbf{V}_{\varphi\varphi} + \alpha n \mathbf{V}_{x\varphi}. \end{aligned} \tag{13}$$

The perturbation field is subject to the no-slip, isothermal boundary conditions $\hat{u}(0) = \hat{v}(0) = \hat{w}(0) = \hat{T}(0) = 0$ at the wall and attenuation conditions $\hat{\phi} \rightarrow 0$ as $y \rightarrow \infty$. If the instability is of the inviscid nature for which the viscosity is secondary, (12) can be approximated by the Rayleigh equation

$$\mathbf{B} \frac{\partial \hat{\phi}}{\partial y} + (-i\omega \Gamma + i\alpha \mathbf{A} + in \mathbf{C} + \mathbf{D}) \hat{\phi} = 0. \tag{14}$$

The system (14) can be recast to the differential equations about \hat{v} and \hat{p} , and the boundary conditions read $\hat{v}(0) = 0$ and $\hat{p}(\infty) \rightarrow 0$. The Malik’s scheme²⁹ is employed to solve the linear systems (12) and (14). In this paper, we are interested in the evolution of the Mack first modes with $|n/(\alpha_r r_0)| < \sqrt{M^2 - 1}$, which are of the inviscid nature.

2. Nonlinear parabolized stability equations

In order to take into account the non-parallelism and the nonlinearity of the finite-amplitude perturbations, we need to solve equation (10) numerically. The computation could be rather efficient if the ∂_{xx} terms, which are indeed small numerically, are neglected, which leads to the NPSE approach.^{12,30} Performing Fourier transform on $\tilde{\phi}$ and \mathbf{F} with respect to φ and t , we obtain

$$\begin{aligned} \tilde{\phi}(x, y, z, t) &= \sum_{M=-M_e}^{M_e} \sum_{N=-N_e}^{N_e} \tilde{\phi}_{MN}(x, y) \exp[i(Nn_0\varphi - M\omega_0 t)], \\ \mathbf{F}(x, y, z, t) &= \sum_{M=-M_e}^{M_e} \sum_{N=-N_e}^{N_e} \tilde{\mathbf{F}}_{MN}(x, y) \exp[i(Nn_0\varphi - M\omega_0 t)]. \end{aligned} \tag{15}$$

Considering that the perturbations are propagating with two length scales, a fast one with an oscillatory manner and a slow one related to the non-parallelism, we express the disturbance $\tilde{\phi}$ as a Wentzel–Kramers–Brillouin (WKB) form Fourier series

$$\tilde{\phi}_{MN}(x, y) = \tilde{\phi}_{MN}(x, y) \exp\left(i \int_{x_0}^x \alpha_{MN} d\bar{x}\right), \quad (16)$$

where the shape function $\tilde{\phi}_{MN}$ varies slowly with x , each Fourier component is denoted as (M, N) , ω_0 and n_0 are the fundamental frequency and circumferential wavenumber, and α_{MN} represents the complex streamwise wavenumber of (M, N) , respectively. x_0 is a streamwise position that is selected as the inlet of the computational domain of the NPSE calculations. Here, we choose $x_0 = R$, such that the inlet of the computation domain corresponds to $X = 1$. M_e and N_e are the upper limit of the order of the truncated Fourier series. In this paper, we choose $M_e = 7$ and $N_e = 10$, which are confirmed to be sufficient for the considered cases.

Neglecting the second-order derivative of $\tilde{\phi}_{MN}$ with respect to x , system (10) is reduced to

$$\frac{\tilde{\mathbf{A}}_{MN} \partial \tilde{\phi}_{MN}}{\partial x} + \frac{\tilde{\mathbf{B}}_{MN} \partial \tilde{\phi}_{MN}}{\partial y} + \mathbf{V}_{yy} \frac{\partial^2 \tilde{\phi}_{MN}}{\partial y^2} + \tilde{\mathbf{D}}_{MN} \tilde{\phi}_{MN} = \tilde{\mathbf{F}}_{MN}. \quad (17)$$

The matrices $\tilde{\mathbf{A}}_{MN}$, $\tilde{\mathbf{B}}_{MN}$, and $\tilde{\mathbf{D}}_{MN}$ are given by

$$\begin{aligned} \tilde{\mathbf{A}}_{MN} &= \mathbf{A} - 2i\alpha_{MN} \mathbf{V}_{xx} - iNn_0 \mathbf{V}_{x\varphi}, \\ \tilde{\mathbf{B}}_{MN} &= \mathbf{B} - i\alpha_{MN} \mathbf{V}_{xy} - iNn_0 \mathbf{V}_{y\varphi}, \\ \tilde{\mathbf{D}}_{MN} &= -iM\omega_0 \Gamma + i\alpha_{MN} \mathbf{A} + iNn_0 \mathbf{C} + \mathbf{D} + N^2 n_0^2 \mathbf{V}_{\varphi\varphi} \\ &\quad + \left(\alpha_{MN}^2 - i \frac{d\alpha_{MN}}{dx}\right) \mathbf{V}_{xx} + N\alpha_{MN} n_0 \mathbf{V}_{x\varphi}, \\ \tilde{\mathbf{F}}_{MN} &= \tilde{\mathbf{F}}_{MN} \exp\left(-i \int_{x_0}^x \alpha_{MN} d\bar{x}\right). \end{aligned} \quad (18)$$

3. Numerical details of the NPSE calculations for the oblique-mode breakdown

In each NPSE calculation, we introduce a pair of oblique Mack first modes with the same frequency but opposite wave angles at $x = x_0$ ($X = 1$), labeled by $(1, \pm 1)$, as the inflow conditions

$$\tilde{\phi} = \varepsilon_{1,1} \hat{\phi}_{1,1}(y) E_{1,1} + \varepsilon_{1,-1} \hat{\phi}_{1,-1}(y) E_{1,-1} + c.c., \quad (19)$$

where $E_{M,N} = \exp[i(\int_{x_0}^x \alpha(x) dx + Nn_0\varphi - M\omega_0 t)]$, and $\varepsilon_{M,N}$ measures the amplitude of each mode. In our paper, we assume the two modes are of inviscid nature, and thus, $\alpha \sim n_0/r_0 \sim \omega \sim 1$. $\hat{\phi}_{1,1}$ and $\hat{\phi}_{1,-1}$ are obtained by solving O–S equation (12), or solving Rayleigh equation (14) to leading-order approximation. The nonlinear interaction between components (1,1) and (1,–1) will generate high-order harmonic modes ($|M| + |N| \geq 2$) and the mean-flow distortion ($M = N = 0$), and the wall-normal boundary conditions for each mode (M, N) read

$$\begin{aligned} (\tilde{u}_{MN}, \tilde{v}_{MN}, \tilde{w}_{MN}, \tilde{T}_{MN}) &= (0, 0, 0, 0) \quad \text{at } y = 0, \\ (\tilde{u}_{MN}, \tilde{v}_{MN}, \tilde{w}_{MN}, \tilde{T}_{MN}) &\rightarrow (0, 0, 0, 0) \quad \text{as } y \rightarrow \infty. \end{aligned} \quad (20)$$

In Eq. (17), because α_{MN} is also unknown, an additional condition is required to close the system

$$\int_0^\infty \rho_B \left(\tilde{u}_{MN}^\dagger \frac{\partial \tilde{u}_{MN}}{\partial x} + \tilde{v}_{MN}^\dagger \frac{\partial \tilde{v}_{MN}}{\partial x} + \tilde{w}_{MN}^\dagger \frac{\partial \tilde{w}_{MN}}{\partial x} \right) dy = 0, \quad (21)$$

where the superscript \dagger denotes the complex conjugate. In the numerical process, α_{MN} is obtained by using an iterative approach

$$\alpha_{MN}^{new} = \alpha_{MN}^{old} - \frac{i}{E_{MN}} \int_0^\infty \rho_B \left(\tilde{u}_{MN}^\dagger \frac{\partial \tilde{u}_{MN}}{\partial x} + \tilde{v}_{MN}^\dagger \frac{\partial \tilde{v}_{MN}}{\partial x} + \tilde{w}_{MN}^\dagger \frac{\partial \tilde{w}_{MN}}{\partial x} \right) dy, \quad (22)$$

where $E_{MN} = \int_0^\infty \rho_B (|\tilde{u}_{MN}|^2 + |\tilde{v}_{MN}|^2 + |\tilde{w}_{MN}|^2) dy$. Note that (22) is not applied to the mean-flow distortion (MFD), for which $M = N = 0$, implying that the growth of the MFD is reflected by the growth of the modulus of its shape function, rather than its complex wavenumber. In our calculations, the iteration continues until the error in relative to the last iterative step is less than 10^{-7} .

The detail of the discretization scheme can be found in Appendix B. At each streamwise location, discretization of system (17) ultimately yields a system of algebraic equations of a generic form

$$L_{MN} \tilde{\phi}_{MN} = R_{MN} + \tilde{\mathbf{F}}_{MN}, \quad (23)$$

where R_{MN} , denoting the inhomogeneous terms due to parabolized operator, is known, but the nonlinear term $\tilde{\mathbf{F}}_{MN}$ is unknown. Therefore, an iterative procedure for $\tilde{\mathbf{F}}_{MN}$ is needed; see Ref. 31. The amplitude of each Fourier mode (M, N) can be defined as

$$A_\phi(x) = \max_y |\tilde{\phi}_{MN}(x, y) + c.c.|. \quad (24)$$

Additionally, if $\tilde{\mathbf{F}}_{MN}$ is set to be zero, Eq. (17) is recast to the linear parabolized stability equations (LPSE), which can be used to track the evolution of each mode separately. The validation of our NPSE code is shown in Appendix C.

III. NUMERICAL RESULTS FOR THE OBLIQUE-MODE BREAKDOWN

A. Base flow and linear instability

In this paper, the computational parameters are listed in Table I. The base-flow profiles for U_B and T_B at three streamwise stations are plotted in Fig. 2, where the generalized inflectional points (GIPs), defined by the positions where $(\rho_B U_{B,y})_y = 0$, are shown by the circles. Figure 3(a) shows the growth-rate contours in the $\Phi - \omega$ planes at $X = 1$, where $\Phi = \tan^{-1}(n/\alpha r_0)$. The greatest growth rate appears at $\omega = 0.117$ and $\Phi = 36^\circ$. Four representative Fourier modes with the same frequency $\omega = 0.117$, but different wave angles $\Phi (= \pm 52^\circ, \pm 36^\circ)$, marked by red dots, are selected. The wave angles of all the selected modes are smaller than $\tan^{-1} \sqrt{M^2 - 1}$, which, according to Smith,⁵ belongs to the inviscid nature. In panel (b), we

TABLE I. Parameters characterizing the flow condition.

M	R	Pr	γ	T_e^* (K)	T_w^* (K)	θ ($^\circ$)	δ^* (mm)	x_0^* (mm)	$x_0 \equiv x_0^*/\delta^*$
3	1170	0.72	1.4	52	300	7	0.117	137	1170

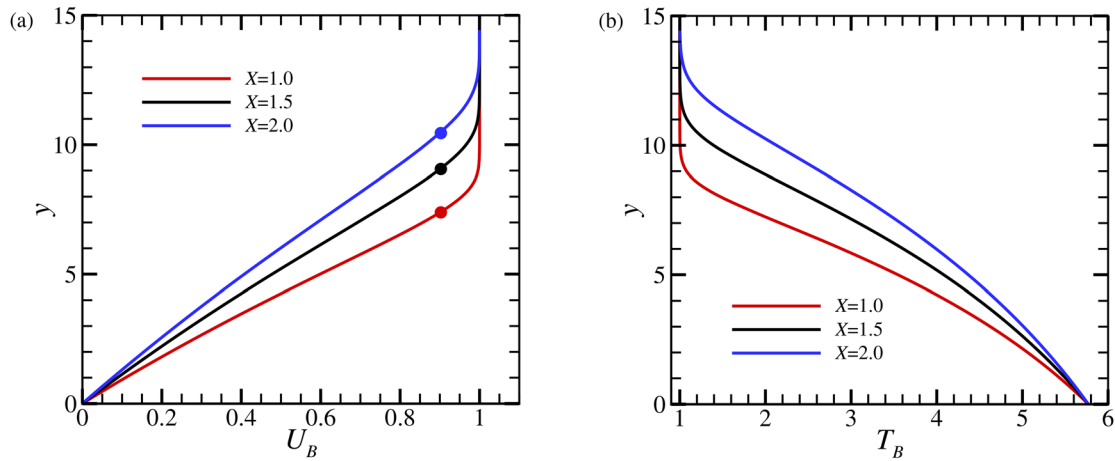


FIG. 2. Base-flow profile of U_B (a) and T_B (b) at $X = 1$, $X = 1.5$, and $X = 2$, where the circles represent the positions of the GIPs.

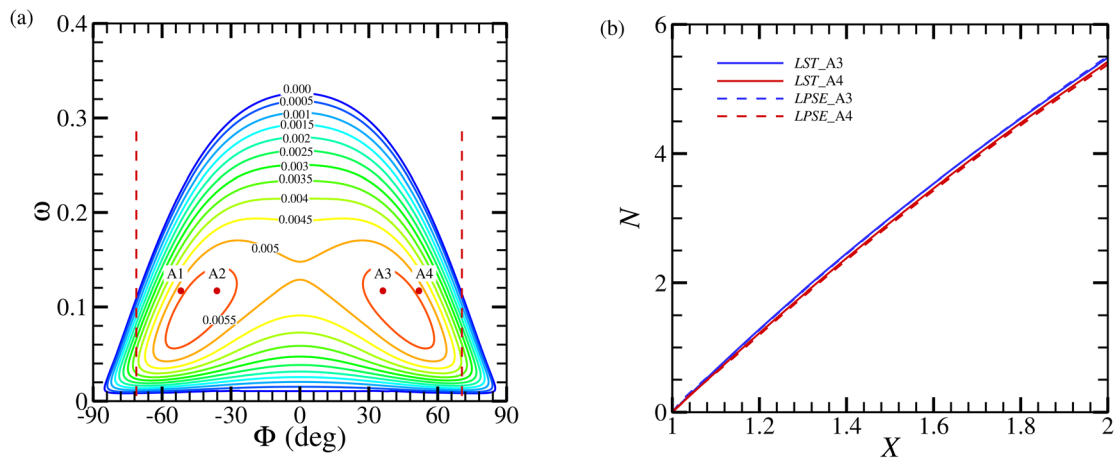


FIG. 3. The linear growth rate at $X = 1$ (a) and the comparison of the N factor obtained by the LST and LPSE predictions (b) of the Mack first mode. The red dashed lines in (a) denote $|\Phi| = \tan^{-1} \sqrt{M^2 - 1}$.

plot the amplitude evolution of modes A3 and A4, which is defined by either the LST, $N(x) = \int_{x_0}^x -\alpha_i(\tilde{x})d\tilde{x}$, or the LPSE, $N(x) = \ln [A_u(x)/A_u(x_0)]$. The difference of the N factor between the LST and LPSE calculations for each mode is rather limited, indicating that the nonparallel effect plays a minor role.

B. Nonlinear development of a pair of first modes

Two cases with different initial perturbations, as listed in Table II, are selected for the NPSE calculations in order to show the oblique-mode breakdown process. Figure 4(a) plots the A_u -evolution of each Fourier component, marked by (M,N), for case I. The evolution of (1,1) agrees with the LPSE prediction until $X = 1.36$, showing a linear feature for the majority of the laminar phase. The growth of the streak mode (0,2) is mainly attributed to the direct interaction of (1,1) and (1,-1). It shows a superexponential growth in the close neighborhood of the inlet, followed by a growth rate that is twice of the fundamental modes (1, ±1); although it is preliminarily small, its high growth

ensures its dominant role for $X > 1.28$. The component (1,3) grows with a rate that is tripled of (1,1), because it is driven by the nonlinear interaction of (1,1) and (0,2). Because it is rather tiny initially, the component (1,3) overwhelms (1,1) at a much later position. The two-dimensional component (2,0), also driven by the direct interaction of (1,1) and (1,-1), shows the same growth rate as that of (0,2), but its amplitude is not as large as the component (0,2) because of its weaker amplification near the inlet. The component (2,2), the harmonic mode

TABLE II. Parameters of introduced oblique modes for the NPSE calculations.

Case	Unstable modes	ω_0	n_0	Label	ε
I	A2	0.117	15	(1,-1)	0.001
	A3			(1,1)	
II	A1	0.117	25	(1,-1)	0.001
	A4			(1,1)	

Downloaded from http://pubs.aip.org/phf/article-pdf/doi/10.1063/5.0117622/16581177/104110_1_online.pdf

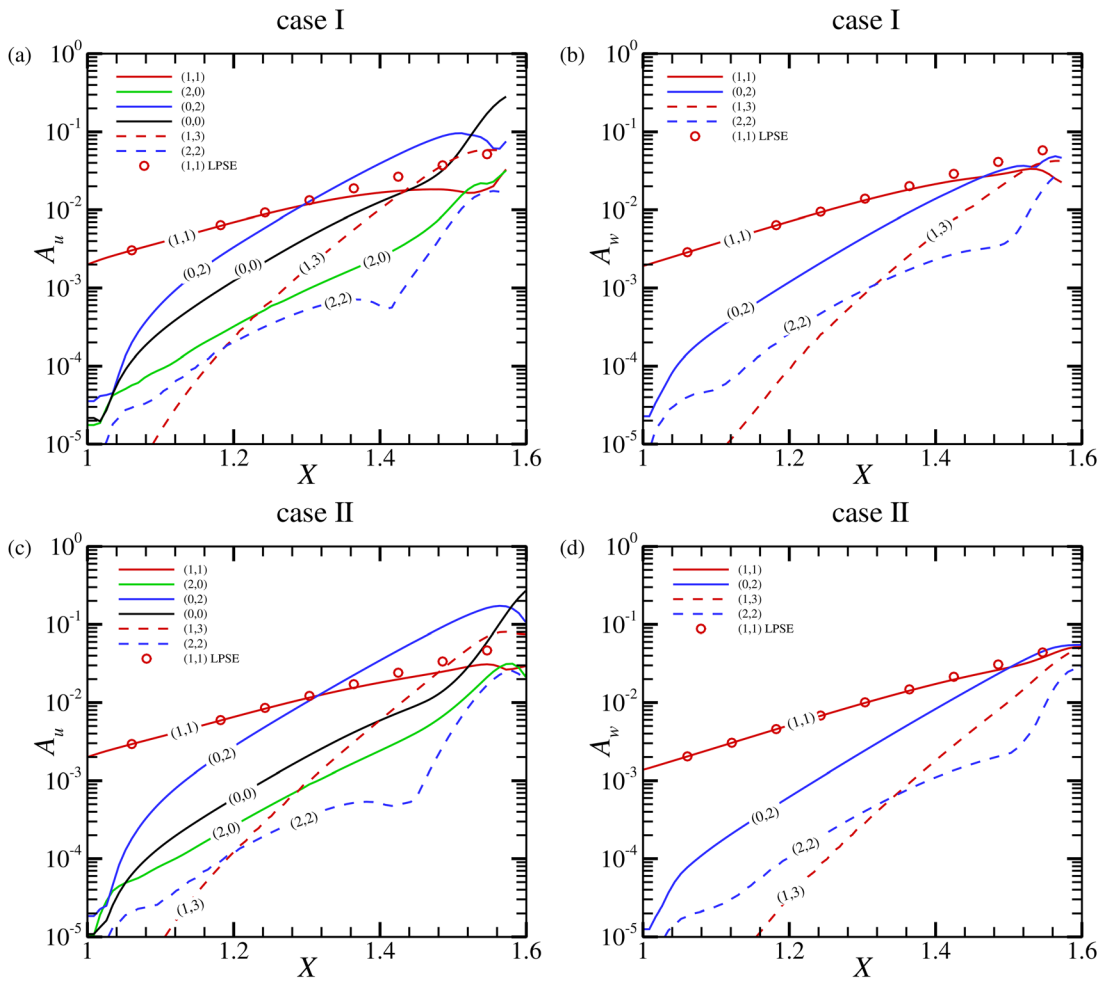


FIG. 4. The evolution of each Fourier components obtained by NPSE. (a) A_u for case I; (b) A_w for case I; (c) A_u for case II; and (d) A_w for case II.

of (1,1), also shows a doubled growth rate as (1,1) for $X < 1.36$, which is however followed by an almost quadrupled growth rate due to the nonlinear forcing of (0,2) and (2,0). These observations agree with that in the oblique-breakdown calculation of Chang and Malik.¹² Such phenomena also apply to case II as shown in panel (c). We also plot the A_w -evolution of each Fourier mode component for cases I and II as shown in panels (b) and (d), respectively. The oblique components show the same property as those of A_u , as shown in panels (a) and (b); however, for the streak mode (0,2), A_w is much smaller than A_u . For the majority of the laminar phase, A_u of the MFD (0,0) grows with the same rate as components (0,2) and (2,0), and its amplitude is between the two components. However, the MFD undergoes a greater amplification when $X > 1.44$ (1.52) for case I (II).

Figure 5 shows the instantaneous contours of u in the φ - X plane at fixed three $\bar{y} = y/\sqrt{X}$ values for case I. Here, \bar{y} is introduced to accommodate the growth of the boundary-layer thickness. The high- and low-speed streaks mainly form in the near-wall region and emerge obviously at around $X = 1.36$, which agrees with the dominant role of (0,2) at $X \approx 1.30$. Different from the streaks, the short-wavelength

waves appear far from the wall as shown in panel (c). For $X < 1.44$, the perturbation field is dominated by the fundamental mode (1,1), followed by a smaller-scale ripples until $X \approx 1.48$, which is reminiscent of (1,3). Such an observation also agrees with the fact A_u of (1,3) overwhelms (1,1) at $X \approx 1.44$ in Fig. 4.

IV. EXPLANATION OF THE EXTRA AMPLIFICATION OF THE STREAK MODES

The nonlinear interaction of the introduced oblique modes (19) would lead to the generation of a series of harmonic modes. Now, we perform the weakly nonlinear analysis (WNA) to probe the perturbations that are driven by the direct interaction of the oblique modes

$$\begin{aligned} &\varepsilon_{1,1}\varepsilon_{1,-1}\check{\phi}_3(y; X) \exp \left[-2 \int \alpha_i(x) dx + 2in_0\varphi \right] \\ &+ \varepsilon_{1,1}\varepsilon_{1,-1}\check{\phi}_4(y; X) \exp \left[2i \left(\int \alpha(x) dx - \omega t \right) \right] \\ &+ O(\varepsilon_{1,1}^2, \varepsilon_{1,-1}^2) + o(\varepsilon_{1,1}\varepsilon_{1,-1}) + \text{c.c.}, \end{aligned} \quad (25)$$

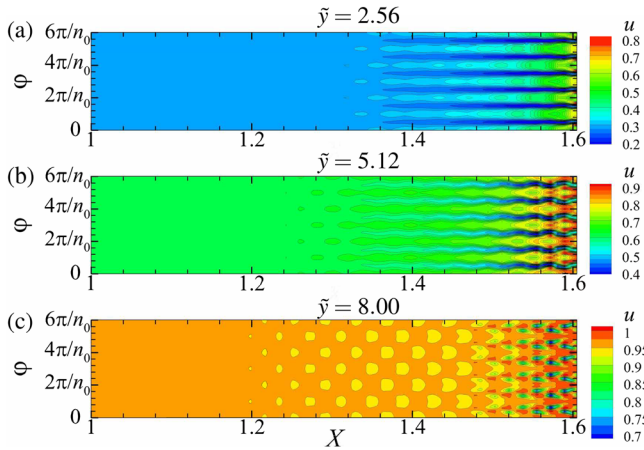


FIG. 5. Contours of the instantaneous u -velocity in the X - φ plane at $\tilde{y} = 2.56$ (a), 5.12 (b), and 7.20 (c) for case I.

where $\tilde{\phi}_3, \tilde{\phi}_4$ represent the shape functions of two harmonic modes, respectively. The first perturbation $\tilde{\phi}_3$ behaves as a stationary, longitudinal streak mode, while the second perturbation $\tilde{\phi}_4$ behaves as a two-dimensional (2D) traveling wave. Note that for an unstable Mack mode, we have $-\alpha_i \ll \alpha_r = O(1)$. For convenience, we introduce $\sigma = -2\alpha_i \ll 1$.

A. Streak mode

In the high- R approximation, the inviscid Mack modes show a double-deck structure, namely, a main layer where $y = O(1)$ and a viscous Stokes layer where $y = O(R^{-1/2})$.^{9,28} For the present configuration, the stokes layer is passive and we focus on the evolution in the main layer. Substituting (19) and (25) into the system (10) and collecting the $O(\varepsilon_{1,1}\varepsilon_{1,-1}) \exp(2in_0\varphi)$ terms, we obtain

$$\sigma U_B M^2 \tilde{p}_3 + \sigma \tilde{u}_3 + \tilde{v}_{3,y} + 2i\beta \tilde{w}_3 = \hat{F}_3^{(1)}, \quad (26a)$$

$$\rho_B (\sigma U_B \tilde{u}_3 + U_{B,y} \tilde{v}_3) + \sigma \tilde{p}_3 = \hat{F}_3^{(2)}, \quad (26b)$$

$$\rho_B \sigma U_B \tilde{v}_3 + \tilde{p}_{3,y} = \hat{F}_3^{(3)}, \quad (26c)$$

$$\rho_B (\sigma U_B \tilde{w}_3) + 2i\beta \tilde{p}_3 = \hat{F}_3^{(4)}, \quad (26d)$$

where we have put $\beta = n_0/r_0$ and $\hat{F}_3^{(1)}$ to $\hat{F}_3^{(4)}$ represent the nonlinear terms. Taking $\hat{\phi}_{1,1}, \hat{\phi}_{1,-1}$ and the inhomogeneous forcing terms $\hat{F}_3^{(1)}$ to $\hat{F}_3^{(4)}$ are all $O(1)$, we find from (26d) that $\tilde{w}_3 \sim 1/\sigma$. Balance of the continuity equation leads to $\tilde{u}_3 \sim 1/\sigma^2$ and $\tilde{v}_3 \sim 1/\sigma$. From (26c), we find that \tilde{p}_3 is at most $O(1)$. Such scalings ensure that the nonlinear terms and pressure gradients in (26a) and (26b) do not appear in the leading order, but those in (26c) and (26d) do.

Now, we re-express the perturbation field of the streak mode as

$$\tilde{\phi}_3 = (\sigma^{-2}\tilde{u}_3, \sigma^{-1}\tilde{v}_3, \sigma^{-1}\tilde{w}_3, \sigma^{-2}\tilde{p}_3, \sigma^{-2}\hat{T}_3, \hat{p}_3)_+, \dots,$$

where $\hat{\phi}_3 \sim 1$; then, the governing equations to the leading order are recast to

$$\hat{u}_3 + \hat{v}_{3,y} + 2i\beta \hat{w}_3 = 0, \quad (27a)$$

$$U_B \hat{u}_3 + U_{B,y} \hat{v}_3 = 0, \quad (27b)$$

$$\rho_B U_B \hat{v}_3 + \hat{p}_{3,y} = \hat{F}_3^{(3)}, \quad (27c)$$

$$\rho_B U_B \hat{w}_3 + 2i\beta \hat{p}_3 = \hat{F}_3^{(4)}, \quad (27d)$$

where $\hat{F}_3^{(3)}$ and $\hat{F}_3^{(4)}$ can be found in Appendix D. The boundary condition for (27) reads

$$\hat{v}_3 = 0 \text{ at } y = 0, \quad \hat{p}_3 \rightarrow 0 \text{ as } y \rightarrow \infty. \quad (28)$$

In numerical process, we need to calculate $\hat{F}_3^{(3)}$ and $\hat{F}_3^{(4)}$ from the introduced oblique mode beforehand and discretize (27) using Malik's²⁹ approach.

The implication of the above analysis is that the small growth rate σ determines the amplification of the streak mode, namely, $\tilde{w}_3 \sim \tilde{v}_3 \sim \sigma^{-1}$ and $\tilde{u}_3 \sim \sigma^{-2}$. The perturbation of the streamwise velocity is extra amplified by a factor of σ^{-2} , showing a longitudinal-streak nature.

B. Traveling harmonic mode

Similar analysis can also be performed for the unsteady traveling mode $\tilde{\phi}_4$. Being different from the streak mode, the convective term of the traveling wave mode is $\tilde{S} = 2i(\alpha U_B - \omega) = O(1)$ instead of the small factor σU_B as in (26). Therefore, we express the governing equations of $\tilde{\phi}_4$ as

$$M^2 \tilde{S} \tilde{p}_4 + 2i\alpha \tilde{u}_4 + \tilde{v}_{4,y} = \hat{F}_4^{(1)}, \quad (29a)$$

$$\rho_B \tilde{S} \tilde{u}_4 + U_{B,y} \tilde{v}_4 + 2i\alpha \tilde{p}_4 = \hat{F}_4^{(2)}, \quad (29b)$$

$$\rho_B \tilde{S} \tilde{v}_4 + \tilde{p}_{4,y} = \hat{F}_4^{(3)}, \quad (29c)$$

where the nonlinear term from $\hat{F}_4^{(1)}$ to $\hat{F}_4^{(3)}$ are $O(1)$ and can be found in Appendix D. We find that in this system, $\tilde{u}_4 \sim \tilde{v}_4 \sim \tilde{p}_4 \sim 1$. Being different from the stationary streak mode $\tilde{\phi}_3$, there is no extra amplification for $\tilde{\phi}_4$, although it has the same growth rate as the streak mode.

C. WNA predictions and comparison with the NPSE results

It has been shown in Fig. 4 that in the majority of the laminar phase, $X < 1.45$, the streak mode (0,2) and the 2D traveling wave (2,0) share the same growth rate, but the magnitude of their amplitudes A_u is of different orders. This can be readily explained by the WNA in Secs. IV A and IV B. Solving the systems (27) and (29) numerically, we can obtain the evolution of the streak mode (0,2) and the 2D traveling waves (2,0), respectively. The comparisons of the amplitudes A_u and A_w for both the streak and 2D traveling modes obtained by the NPSE calculation and WNA prediction for the two cases are shown in Fig. 6. After a certain adjustment region near $X = 1$, the WNA predictions agree well with the NPSE calculations, and the extra amplification of A_u for the streak mode is well predicted by the WNA method.

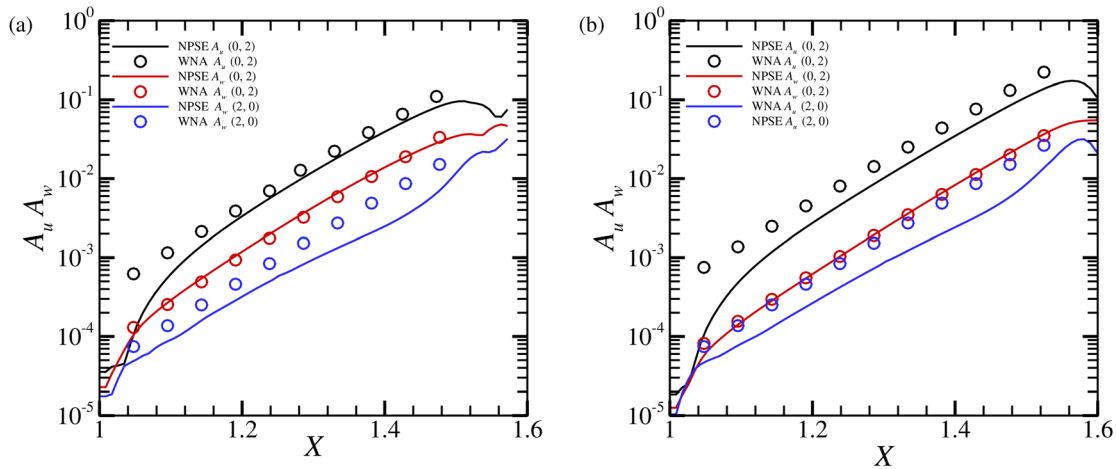


FIG. 6. The comparison of A_u and A_w between the NPSE results and the WNA predictions. Plot (a) case I; and plot (b) case II.

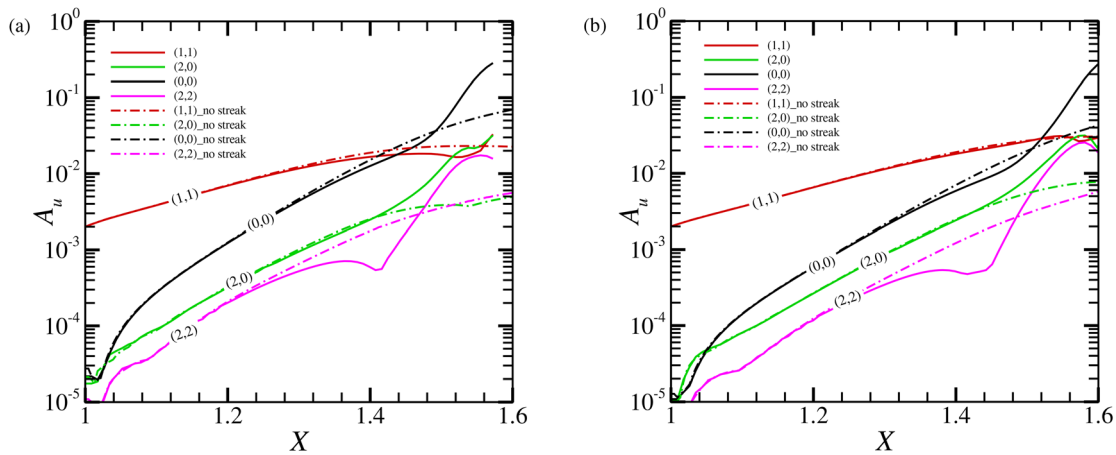


FIG. 7. The comparison of the A_u -evolution between the NPSE calculations and those by artificially removing the streak component. (a) case I; and (b) case II.

V. ROLL OF THE STREAK MODE

Now we probe the impact of the streak mode on the nonlinear evolution of other Fourier components. Figure 7(a) compares the A_u -evolution of each Fourier component with that obtained by removing artificially the streak mode (0,2) for case I. The two families of curves agree with each other before $X \approx 1.24$, where the fundamental mode (1,1) grows almost linearly as confirmed in Fig. 4(a). However, when the streak mode is removed, the sharp amplification of the other components is not seen, indicating the crucial role of the streak mode in the nonlinear phase. This phenomena also appear for case II as shown in panel (b), and the two families of curves deviate at $X \approx 1.28$.

The coefficients of the skin friction, $C_f = \left(\frac{2u}{R} \frac{\partial u}{\partial y}\right)_{y=0}$, are plotted in Fig. 8, where the overbar represents the temporal and circumferential averaging. For both case I and case II, the C_f curves decreases with X gradually at the beginning, agreeing with the unperturbed laminar-flow state. The C_f curve starts to deviate from the laminar state at $X \approx 1.44$ and 1.52, respectively. The two positions correspond to the locations when the MFD components undergo greater growth rates shown in Fig. 4. The sudden increase in the C_f curves lead to the breakdown of

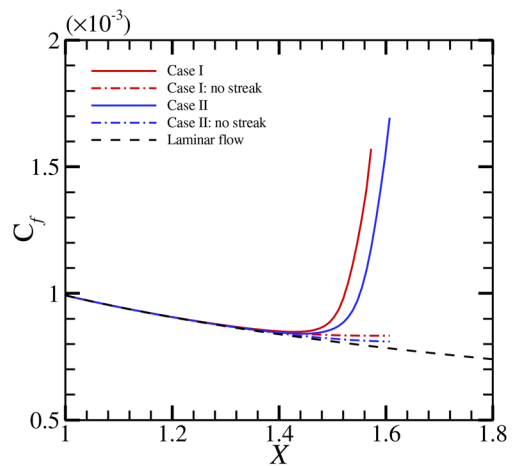


FIG. 8. Comparison of the C_f curves between the NPSE calculations and those by artificially removing the streak component.

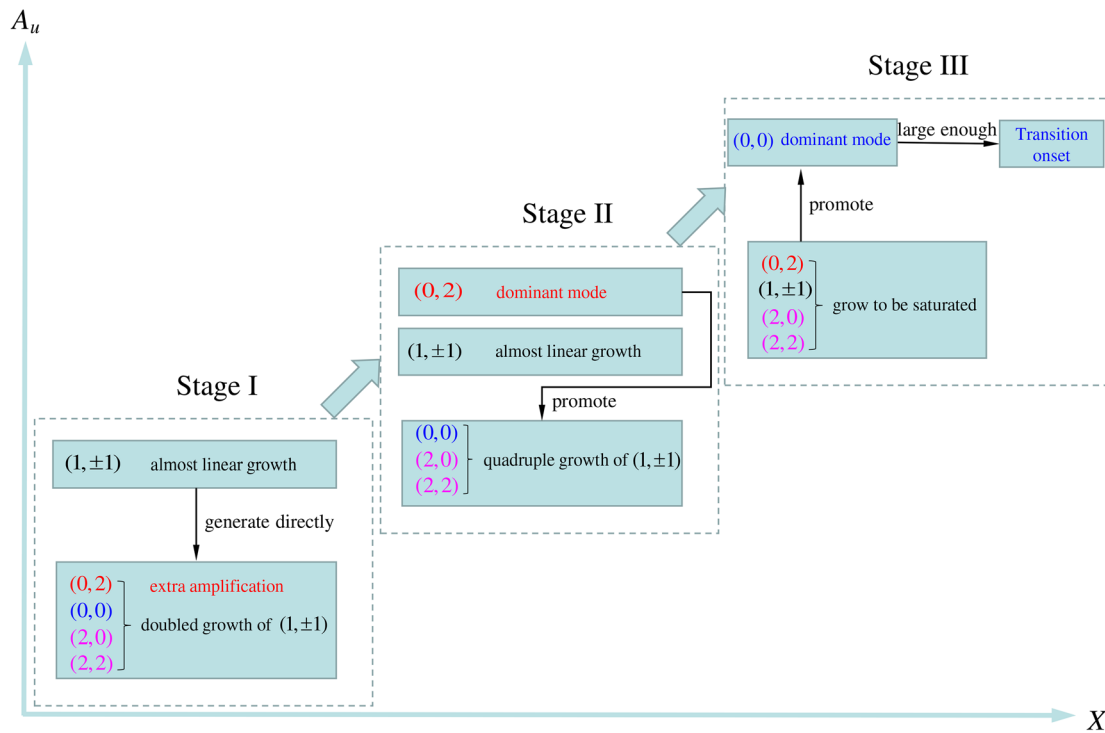


FIG. 9. Sketch of transition process by oblique-mode breakdown.

the laminar flow. The transition onset for case I appears a little earlier, because of the greater growth rate of the introduced perturbations. When the streak mode is removed, the drastic increase in the C_f curve for each case disappears immediately, confirming again the important role of the streak mode. A sketch of transition process by oblique-mode breakdown can be summarized in Fig. 9.

It is then concluded that the streak mode plays a crucial role in triggering the laminar-turbulent transition in the oblique-mode breakdown regime. Although its amplitude is initially small, it undergoes an extra amplification and becomes the dominant perturbation in the late laminar phase. When it reaches a finite amplitude, it serves as the seed for the rapid growth of the small-scale secondary instability modes, which is a reminiscent of the bypass transition.^{32–34} As a consequence, the mean flow is further distorted by the finite-amplitude perturbations due to their forcing in terms of the Reynolds stress, leading to the sudden increase in the C_f curve and breakdown of the laminar flow. Artificially removing the streak mode simply leads to a remarkable postpone of the transition onset. Such a phenomenon was also observed in a subharmonic-resonance study in an incompressible boundary layer.³⁵

VI. SUMMARY AND CONCLUSION

In a low-Mach-number supersonic boundary layer, the oblique-mode breakdown is believed to be the most efficient regime for the laminar-turbulent transition, because the linear instability, the Mack first mode, is the most unstable at a certain oblique wave angle. Although this regime has been studied extensively by numerics and experiments, some phenomena are still unexplained. In this paper, we revisit this regime by considering the evolution of a pair of

finite-amplitude oblique first modes in a Mach 3 supersonic boundary layer over a sharp cone.

From the NPSE calculations, it is confirmed that the streak mode is greatly amplified due to the direct interaction of the introduced oblique modes, and its streamwise velocity perturbation attains an even larger amplitude. This phenomenon is explained by the weakly nonlinear analysis based on the main-layer solutions in the large- R asymptotic framework, and the WNA predictions are confirmed to be sufficiently accurate by comparing with the NPSE calculations.

Indeed, the extra amplified streak mode plays a crucial role in triggering the transition onset, confirmed by comparing with the results with the streak component artificially removed. Therefore, the whole scenario of the oblique-mode breakdown is well understood: (i) the rapid growth of the linear oblique modes leads to an extra amplification of the streak mode, which overwhelms the oblique modes before they reach nonlinear saturation; (ii) the dominant streak mode leads to a rapid amplification of the small-scale secondary instability modes, producing finite Reynolds stress to distort the mean flow; and (iii) the mean-flow distortion starts to increase with an even greater rate than that caused by the direct interaction of the fundamental oblique modes, leading to a drastic increase in the C_f curve. This is considered as the onset of transition to turbulence.

ACKNOWLEDGMENTS

This work was supported by NSFC Basic Science Center Program for “Multiscale Problems in Nonlinear Mechanics” (Grant No. 11988102), National Science Foundation of China (Grant

Nos. 12002235 and U20B2003), and Strategic Priority Research Program, CAS (No. XDB22040104).

AUTHOR DECLARATIONS

Conflict of Interest

The authors have no conflicts to disclose.

Author Contributions

Runjie Song: Data curation (lead); Formal analysis (equal); Investigation (lead); Resources (lead); Validation (lead); Visualization (lead); Writing – original draft (lead). **Ming Dong:** Conceptualization (equal); Formal analysis (equal); Funding acquisition (equal); Project administration (equal); Supervision (equal); Writing – review & editing (equal). **Lei Zhao:** Funding acquisition (equal); Investigation (equal); Methodology (lead); Software (lead).

DATA AVAILABILITY

The data that support the findings of this study are available from the corresponding author upon reasonable request.

APPENDIX A: THE COEFFICIENT MATRICES AND THE NONLINEAR FORCING IN EQUATION (10)

In Eq. (10), Γ , \mathbf{A} , \mathbf{B} , \mathbf{C} , \mathbf{D} , \mathbf{V}_{xx} , \mathbf{V}_{yy} , $\mathbf{V}_{\varphi\varphi}$, \mathbf{V}_{xy} , $\mathbf{V}_{y\varphi}$, and $\mathbf{V}_{x\varphi}$ are 5×5 -order matrices, whose non-zero elements are

$$\begin{aligned} \Gamma_{11} &= 1, \quad \Gamma_{22} = \Gamma_{33} = \Gamma_{44} = \rho_B, \\ \Gamma_{51} &= -\frac{(\gamma - 1)T_B}{\gamma}, \quad \Gamma_{55} = \frac{\rho_B}{\gamma}, \\ A_{11} &= U_B, \quad A_{12} = \rho_B, \quad A_{21} = \frac{T_B}{\gamma M^2}, \\ A_{22} &= \rho_B U_B - \frac{4(g\mu_B + \mu_{B,x})}{3R}, \\ A_{23} &= -\frac{(\mu_B h + \tau T_{B,y})}{R}, \quad A_{25} = \frac{\rho_B}{\gamma M^2} + \frac{2\tau}{R} \left(\frac{1}{3} \nabla \cdot \vec{\mathbf{U}} - S_{11} \right), \\ A_{32} &= \frac{2\mu_{B,y}}{3R}, \quad A_{33} = \rho_B U_B - \frac{(\mu_{B,x} + g\mu_B)}{R}, \quad A_{35} = \frac{-2\tau S_{12}}{R}, \\ A_{44} &= \rho_B U_B - \frac{(g\mu_B + \mu_{B,x})}{R}, \quad A_{51} = -\frac{\gamma - 1}{\gamma} T_B U_B, \\ A_{52} &= -\frac{4(\gamma - 1)M^2}{R} \mu_B \left(S_{11} - \frac{1}{3} \nabla \cdot \vec{\mathbf{U}} \right), \\ A_{53} &= -\frac{4(\gamma - 1)M^2}{R} \mu_B S_{12}, \quad A_{55} = \frac{\rho_B U_B}{\gamma} - \frac{(\tau T_{B,x} + g\mu_B)}{RPr}, \\ B_{11} &= \tilde{V}_B, B_{13} = \rho_B, \quad B_{22} = \rho_B \tilde{V}_B - \frac{(h\mu_B + \mu_{B,y})}{R}, \\ B_{23} &= \frac{2\mu_{B,x}}{3R}, \quad B_{25} = \frac{-2\tau S_{21}}{R}, \quad B_{31} = \frac{T_B}{\gamma M^2}, \\ B_{32} &= -\frac{1}{R} \left(\mu_{B,x} + \frac{1}{3} g\mu_B \right), \quad B_{33} = \rho_B \tilde{V}_B - \frac{4}{3R} (\mu_{B,y} + h\mu_B), \\ B_{35} &= \frac{\rho_B}{\gamma M^2} + \frac{2\mu_{B,T}}{R} \left(\frac{1}{3} \nabla \cdot \vec{\mathbf{U}} - S_{22} \right), \end{aligned}$$

$$\begin{aligned} B_{44} &= \rho_B \tilde{V}_B - \frac{(h\mu_B + \mu_{B,y})}{R}, \\ B_{51} &= -\frac{\gamma - 1}{\gamma} T_B \tilde{V}_B, \quad B_{52} = -\frac{4(\gamma - 1)M^2}{R} \mu_B S_{21}, \\ B_{53} &= -\frac{4(\gamma - 1)M^2}{R} \mu_B \left(S_{22} - \frac{1}{3} \nabla \cdot \vec{\mathbf{U}} \right), \\ B_{55} &= \frac{\rho_B \tilde{V}_B}{\gamma} - \frac{2\mu_{B,y} + h\mu_B}{RPr}, \\ C_{14} &= \frac{\rho_B}{r}, \quad C_{24} = \frac{7g\mu_B}{3rR} + \frac{2\mu_{B,x}}{3rR}, \\ C_{34} &= \frac{(2\mu_{B,y} + 7h\mu_B)}{3rR}, \quad C_{41} = \frac{T_B}{r\gamma M^2}, \\ C_{42} &= -\frac{1}{rR} \left(\frac{7}{3} g\mu_B + \mu_{B,x} \right), \\ C_{43} &= -\frac{1}{rR} \left(\frac{7}{3} h\mu_B + \mu_{B,y} \right), \\ C_{45} &= \frac{\rho_B}{r\gamma M^2} + \frac{2\tau}{rR} \left(\frac{1}{3} \nabla \cdot \vec{\mathbf{U}} - S_{33} \right), \\ C_{54} &= -\frac{4(\gamma - 1)M^2}{rR} \mu_B \left(S_{33} - \frac{1}{3} \nabla \cdot \vec{\mathbf{U}} \right), \\ D_{11} &= \nabla \cdot \vec{\mathbf{U}}, \quad D_{12} = \rho_{B,x} + g\rho_B, \quad D_{13} = \rho_{B,y} + h\rho_B, \\ D_{21} &= \left(U_B U_{B,x} + \tilde{V}_B U_{B,y} \right) + \frac{T_{B,x}}{\gamma M^2}, \\ D_{22} &= \rho_B U_{B,x} + \frac{2g}{3R} (2g\mu_B + \mu_{B,x}), \\ D_{23} &= \rho_B U_{B,y} + \frac{2h}{3R} (2g\mu_B + \mu_{B,x}), \\ D_{25} &= \frac{\rho_{B,x}}{\gamma M^2} - \frac{1}{R} \left\{ \tau \left[\left(2S_{11} - \frac{2}{3} \nabla \cdot \vec{\mathbf{U}} \right)_x + 2S_{21,x} + 2hS_{21} \right. \right. \\ &\quad \left. \left. + 2gS_{11} - 2gS_{33} \right] + \left(2S_{11} - \frac{2}{3} \nabla \cdot \vec{\mathbf{U}} \right) \tau_x + 2S_{21} \tau_y \right\}, \\ D_{31} &= \left(U_B \tilde{V}_{B,x} + \tilde{V}_B \tilde{V}_{B,y} \right) + \frac{T_{B,y}}{\gamma M^2}, \\ D_{32} &= \rho_B \tilde{V}_{B,x} + \frac{2g}{R} \left[\frac{\mu_{B,y}}{3} + \left(h + \frac{g}{3} \right) \mu_B \right], \\ D_{33} &= \rho_B \tilde{V}_{B,y} + \frac{2h}{3R} (2h\mu_B + \mu_{B,y}), \\ D_{35} &= \frac{\rho_{B,y}}{\gamma M^2} - \frac{1}{R} \left\{ \tau \left[2S_{12,x} + \left(2S_{22} - \frac{2}{3} \nabla \cdot \vec{\mathbf{U}} \right)_y + 2hS_{22} \right. \right. \\ &\quad \left. \left. + 2gS_{12} - 2hS_{33} \right] + 2S_{12} \tau_x + \left(2S_{22} - \frac{2}{3} \nabla \cdot \vec{\mathbf{U}} \right) \tau_y \right\}, \\ D_{44} &= \rho_B (gU_B + h\tilde{V}_B) + \frac{1}{R} \left[(g^2 + h^2) \mu_B + \frac{2}{3} g\mu_{B,x} \right], \\ D_{51} &= \frac{1}{\gamma} (\vec{\mathbf{U}} \cdot \nabla T_B), \\ D_{52} &= \frac{\rho_B T_{B,x}}{\gamma} - \frac{4\mu_B (\gamma - 1) M^2 g}{R} \left(S_{33} - \frac{1}{3} \nabla \cdot \vec{\mathbf{U}} \right) - \frac{(\gamma - 1) T_B \rho_{B,x}}{\gamma}, \end{aligned}$$

Downloaded from http://pubs.aip.org/aip/pof/article-pdf/doi/10.1063/5.0117622/1658117/104110_1_online.pdf

$$\begin{aligned}
 D_{53} &= \frac{\rho_B T_{B,y}}{\gamma} - \frac{4\mu_B(\gamma-1)M^2 h}{R} \left(S_{33} - \frac{1}{3} \nabla \cdot \vec{\mathbf{U}} \right) \\
 &\quad - \frac{(\gamma-1)T_B \rho_{B,y}}{\gamma}, \\
 D_{55} &= -\frac{2(\gamma-1)M^2 \tau}{R} \left[\mathbf{S}_B :: \mathbf{S}_B - \frac{1}{3} (\nabla \cdot \vec{\mathbf{U}})^2 \right] \\
 &\quad - \frac{\nabla \cdot (\mu_B \nabla T_B)}{RPr} - \frac{\gamma-1}{\gamma} (\vec{\mathbf{U}} \cdot \nabla \rho_B), \\
 V_{xx,22} &= -\frac{4\mu_B}{3R}, \quad V_{xx,33} = -\frac{\mu_B}{R}, \quad V_{xx,44} = -\frac{\mu_B}{R}, \\
 V_{xx,55} &= -\frac{\mu_B}{RPr}, \quad V_{yy,22} = -\frac{\mu_B}{R}, \quad V_{yy,33} = -\frac{4\mu_B}{3R}, \\
 V_{yy,44} &= -\frac{\mu_B}{R}, \quad V_{yy,55} = -\frac{\mu_B}{RPr}, \quad V_{\varphi\varphi,22} = -\frac{\mu_B}{r^2 R}, \\
 V_{\varphi\varphi,33} &= -\frac{\mu_B}{r^2 R}, \quad V_{\varphi\varphi,44} = -\frac{4\mu_B}{3r^2 R}, \quad V_{\varphi\varphi,55} = -\frac{\mu_B}{r^2 RPr}, \\
 V_{xy,23} &= V_{xy,32} = -\frac{\mu_B}{3R}, \quad V_{x\varphi,24} = V_{x\varphi,42} = -\frac{\mu_B}{3rR}, \\
 V_{y\varphi,34} &= V_{y\varphi,43} = -\frac{\mu_B}{3rR},
 \end{aligned}$$

with $\vec{V}_B = R^{-1} V_B$, $\tau = \frac{d\mu_B}{dI_B}$, $\vec{\mathbf{U}} = [U_B, \vec{V}_B, 0]^T$, $g = \sin\theta/r$, $h = \cos\theta/r$, $\nabla \cdot \vec{\mathbf{U}} = U_{B,x} + \vec{V}_{B,y} + gU_B + h\vec{V}_B$ and \mathbf{S}_B the rate of strain tensor of the base flow, whose components are

$$\begin{aligned}
 S_{11} &= U_{B,x}, \quad S_{22} = \vec{V}_{B,y}, \quad S_{33} = gU_B + h\vec{V}_B, \\
 S_{12} &= S_{21} = (\vec{V}_{B,x} + U_{B,y})/2.
 \end{aligned}$$

\mathbf{F} is a vector, and its elements are

$$\begin{aligned}
 F^{(1)} &= -(\tilde{\rho} \nabla \cdot \vec{\mathbf{u}} + \vec{\mathbf{u}} \cdot \nabla \tilde{\rho}), \\
 F^{(2)} &= -\tilde{\rho} \tilde{u}_t - \tilde{\rho} (U_B \tilde{u}_x + \vec{V}_B \tilde{u}_y + \tilde{u} U_{B,x} + \tilde{v} U_{B,x}) \\
 &\quad - (\tilde{\rho} + \rho_B) (\tilde{u} \tilde{u}_x + \tilde{v} \tilde{u}_y + \tilde{w} \tilde{u}_\varphi / r - g \tilde{w}^2) - \frac{(\tilde{\rho} \tilde{T})_x}{\gamma M^2} \\
 &\quad - \frac{2}{3R} (\tilde{\mu} \nabla \cdot \vec{\mathbf{u}})_x + \frac{2}{R} \left[(\tilde{\mu} \tilde{S}_{11})_x + (\tilde{\mu} \tilde{S}_{21})_y \right. \\
 &\quad \left. + (\tilde{\mu} \tilde{S}_{31})_\varphi / r + \tilde{\mu} (g \tilde{S}_{11} + h \tilde{S}_{21} - g \tilde{S}_{33}) \right], \\
 F^{(3)} &= -\tilde{\rho} \tilde{v}_t - \tilde{\rho} (U_B \tilde{v}_x + \vec{V}_B \tilde{v}_y + \tilde{u} \tilde{v}_{B,x} + \tilde{v} \tilde{v}_{B,y}) \\
 &\quad - (\tilde{\rho} + \rho_B) (\tilde{u} \tilde{v}_x + \tilde{v} \tilde{v}_y + \tilde{w} \tilde{v}_\varphi / r - h \tilde{w}^2_3) - \frac{(\tilde{\rho} \tilde{T})_y}{\gamma M^2} \\
 &\quad - \frac{2}{3R} (\tilde{\mu} \nabla \cdot \vec{\mathbf{u}})_y + \frac{2}{R} \left[(\tilde{\mu} \tilde{S}_{12})_x + (\tilde{\mu} \tilde{S}_{22})_y \right. \\
 &\quad \left. + (\tilde{\mu} \tilde{S}_{32})_\varphi / r + \tilde{\mu} (g \tilde{S}_{12} + h \tilde{S}_{22} - h \tilde{S}_{32}) \right], \\
 F^{(4)} &= -\tilde{\rho} \tilde{w}_t - \tilde{\rho} [U_B \tilde{w}_x + \vec{V}_B \tilde{w}_y + g \tilde{w} U_B + h \tilde{w} V_B] \\
 &\quad - (\tilde{\rho} + \rho_B) (\tilde{u} \tilde{w}_x + \tilde{v} \tilde{w}_y + \tilde{w} \tilde{w}_\varphi / r + g \tilde{u} \tilde{w} + h \tilde{v} \tilde{w}) \\
 &\quad - \frac{(\tilde{\rho} \tilde{T})_\varphi}{\gamma r M^2} - \frac{2}{3rR} (\tilde{\mu} \nabla \cdot \vec{\mathbf{u}})_\varphi + \frac{2}{R} \left[(\tilde{\mu} \tilde{S}_{13})_x + (\tilde{\mu} \tilde{S}_{23})_y \right. \\
 &\quad \left. + (\tilde{\mu} \tilde{S}_{33})_\varphi / r + 2\tilde{\mu} (g \tilde{S}_{13} + h \tilde{S}_{23}) \right],
 \end{aligned}$$

$$\begin{aligned}
 F^{(5)} &= -\frac{\tilde{\rho}}{\gamma} (\tilde{T}_t + \vec{\mathbf{u}} \cdot \nabla T_B + \vec{\mathbf{U}} \cdot \nabla \tilde{T} + \vec{\mathbf{u}} \cdot \nabla \tilde{T}) \\
 &\quad + (\gamma-1)M^2 \left\{ 2\tilde{\mu} \tilde{\mathbf{S}} :: \tilde{\mathbf{S}} - \frac{2}{3} \tilde{\mu} (\nabla \cdot \vec{\mathbf{u}})^2 \right\} \\
 &\quad + \frac{\gamma-1}{\gamma} \tilde{T} (\tilde{\rho}_t + \vec{\mathbf{u}} \cdot \nabla \rho_B + \vec{\mathbf{U}} \cdot \nabla \tilde{\rho} + \vec{\mathbf{u}} \cdot \nabla \tilde{\rho}) \\
 &\quad + (\gamma-1)M^2 \left[2\mu_B \tilde{\mathbf{S}} :: \tilde{\mathbf{S}} - \frac{2}{3} \mu_B (\nabla \cdot \vec{\mathbf{u}})^2 \right. \\
 &\quad \left. + 4\tilde{\mu} \tilde{\mathbf{S}} :: \tilde{\mathbf{S}} - \frac{4}{3} \tilde{\mu} (\nabla \cdot \vec{\mathbf{U}}) (\nabla \cdot \vec{\mathbf{u}}) \right] + \frac{\gamma-1}{\gamma} T_B (\vec{\mathbf{u}} \cdot \nabla \tilde{\rho}) \\
 &\quad - \frac{\rho_B}{\gamma} (\vec{\mathbf{u}} \cdot \nabla \tilde{T}) + \nabla \cdot (\tilde{\mu} \nabla \tilde{T}),
 \end{aligned}$$

with $\vec{\mathbf{u}} = [\tilde{u}, \tilde{v}, \tilde{w}]^T$, $\nabla \cdot \vec{\mathbf{u}} = (\tilde{u}_x + \tilde{v}_y + \tilde{w}_\varphi / r + g \tilde{u} + h \tilde{v})$ and $\tilde{\mathbf{S}}$ the rate of strain tensor of disturbance, whose six dependent components are

$$\begin{aligned}
 \tilde{S}_{11} &= \tilde{u}_x, \quad \tilde{S}_{22} = \tilde{v}_y, \quad \tilde{S}_{33} = \tilde{w}_\varphi / r + g \tilde{u} + h \tilde{v}, \\
 \tilde{S}_{12} &= \tilde{S}_{21} = (\tilde{v}_x + \tilde{u}_y) / 2, \\
 \tilde{S}_{13} &= \tilde{S}_{31} = (\tilde{w}_x + \tilde{u}_\varphi / r - g \tilde{w}) / 2, \\
 \tilde{S}_{23} &= \tilde{S}_{32} = (\tilde{w}_y + \tilde{v}_\varphi / r - h \tilde{w}) / 2.
 \end{aligned}$$

APPENDIX B: DISCRETIZATION OF THE NPSE

The rectangular mesh system is employed for the NPSE calculation, which is uniform in the streamwise direction but clustered in the near-wall region in the transverse direction. Each grid point is denoted by (i, j) , with $i \in [0, I]$ and $j \in [0, J]$. The streamwise derivative is discretized as

$$\begin{aligned}
 \frac{\partial \hat{\phi}_{MN,i}}{\partial x} &= \frac{3\hat{\phi}_{MN,i} - 4\hat{\phi}_{MN,i-1} + \hat{\phi}_{MN,i-2}}{2\Delta x}, \quad \text{for } i > 1, \\
 \frac{\partial \hat{\phi}_{MN,i}}{\partial x} &= \frac{\hat{\phi}_{MN,i} - \hat{\phi}_{MN,i-1}}{\Delta x}, \quad \text{for } i = 1,
 \end{aligned} \tag{B1}$$

where Δx is the grid spacing in the streamwise direction. The non-uniform transverse coordinate y is mapped into a uniform computational coordinate η , and $\partial/\partial y$ and $\partial^2/\partial y^2$ are recast to

$$\frac{\partial}{\partial y} = \eta_y \frac{\partial}{\partial \eta}, \quad \frac{\partial}{\partial y^2} = \eta_{yy} \frac{\partial}{\partial \eta} + \eta_y^2 \frac{\partial^2}{\partial \eta^2}. \tag{B2}$$

Thus, the wall-normal derivative is discretized as

$$\begin{aligned}
 \frac{\partial \phi_{MN,j}}{\partial \eta} &= \frac{1}{\Delta \eta} \sum_{k=j-2}^{k=j+2} c_k \phi_{MN,k}, \\
 \frac{\partial \phi_{MN,j}}{\partial \eta} &= \frac{1}{\Delta \eta} \sum_{k=j-2}^{k=j+2} d_k \phi_{MN,k},
 \end{aligned} \tag{B3}$$

where c_j and d_j can be found in Tables III and IV, respectively. The order-of-accuracy for different choices of c_j and d_j is also given in the tables. In this paper, we choose the number of the grid points in the wall-normal direction to be $J = 580$, and the grid points are allocated as

TABLE III. Difference of scheme coefficient c_j for the first derivative.

j	c_{j-2}	c_{j-1}	c_j	c_{j+1}	c_{j+2}	Order
0	0	0	-3/2	2	-1/2	2
1	0	-1/3	-1/2	1	-1/6	3
$[2, J - 2]$	1/12	-2/3	0	2/3	-1/12	4
$J - 1$	1/6	-1	1/2	1/3	0	3
J	1/2	-2	3/2	0	0	2

TABLE IV. Difference of scheme coefficient d_j for the second derivative.

j	d_{j-2}	d_{j-1}	d_j	d_{j+1}	d_{j+2}	Order
0	0	0	1	-2	1	1
1	0	1	-2	1	1	2
$[2, J - 2]$	-1/12	4/3	-5/2	4/3	-1/12	3
$J - 1$	0	1	-2	1	0	2
J	1	-2	1	0	0	1

$$\frac{y_j}{\delta_{99}} = \frac{aj/J}{1 + a/\bar{y}_j - j/J}, \quad a = \frac{\bar{y}_J}{\bar{y}_J - 2}, \quad \bar{y}_J = y_J/\delta_{99}, \quad (B4)$$

where δ_{99} denotes the nominal boundary-layer thickness at the inlet of the computational domain.

APPENDIX C: VALIDATION OF THE NPSE CODE

In order to verify our NPSE code, we repeat the case study of Chang and Malik,¹² in which a two-dimensional wave [mode (2,0)] with a frequency of $\omega = 0.0208$ and two pairs of three-dimensional disturbances with equal spanwise wavenumbers of $\beta = 0.04992$ and frequencies of 0.0208 [mode (2,1) and (2, -1)] and 0.0104 [mode (1,1) and (1, -1)] are introduced at $R_x = 520$ in a Mach 1.6

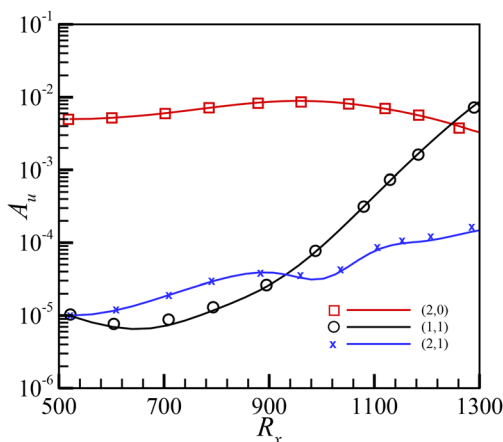


FIG. 10. Comparison of the evolution of the representative Fourier components of our NPSE calculations with those in Ref. 12.

flat-plate boundary layer, where $R_x = \sqrt{\frac{\rho_\infty u_\infty x}{\mu_\infty}}$. As shown in Fig. 10, our calculations of the Fourier components (2,0), (2,1), and (1,1) agree well with those in Ref. 12, confirming the accuracy of our NPSE code.

APPENDIX D: NONLINEAR TERMS IN THE WNA EQUATIONS (27) AND (29)

$$\hat{F}_3^{(3)} = -2 \left\{ \hat{\rho}_{1,1} \left[(i\alpha)^\dagger U_B (\hat{v}_{1,1})^\dagger + (i\omega) (\hat{v}_{1,1})^\dagger \right] \right\}_r - 2\rho_B \left[(i\alpha)^\dagger \hat{u}_{1,1} (\hat{v}_{1,1})^\dagger + \hat{v}_{1,1} (\hat{v}_{1,1}^\dagger)_y \right]_r - 2\rho_B [(i\beta) \hat{w}_{1,1} (\hat{v}_{1,1})^\dagger]_r, \quad (D1)$$

$$\hat{F}_3^{(4)} = 2 \left\{ \hat{\rho}_{1,1} \left[(i\omega) \hat{w}^\dagger_{1,1} + (i\alpha)^\dagger U_B \hat{w}^\dagger_{1,1} \right] \right\}_i + 2\rho_B \left[(i\alpha)^\dagger \hat{u}_{1,1} (\hat{w}_{1,1})^\dagger + \hat{v}_{1,1} (\hat{w}_{1,1}^\dagger)_y \right]_i + 2\rho_B [(i\beta) \hat{w}_{1,1} (\hat{w}_{1,1})^\dagger].$$

$$\hat{F}_4^{(1)} = -2M^2 [(i\alpha) \hat{u}_{1,1} \hat{p}_{1,1} + \hat{v}_{1,1} (\hat{p}_{1,1})_y - (i\beta) \hat{w}_{1,1} \hat{p}_{1,1}],$$

$$\hat{F}_4^{(2)} = -2\rho_B [(i\alpha) \hat{u}_{1,1}^2 + \hat{v}_{1,1} (\hat{u}_{1,1})_y - (i\beta) \hat{w}_{1,1} \hat{u}_{1,1}] + 2\hat{\rho}_{1,1} [(i\omega) \hat{u}_{1,1} - (i\alpha) U_B \hat{u}_{1,1} - U_{B,y} \hat{v}_{1,1}], \quad (D2)$$

$$\hat{F}_4^{(3)} = -2\rho_B [(i\alpha) \hat{u}_{1,1} \hat{v}_{1,1} + \hat{v}_{1,1} (\hat{v}_{1,1})_y - (i\beta) \hat{w}_{1,1} \hat{v}_{1,1}] + 2\hat{\rho}_{1,1} [(i\omega) \hat{v}_{1,1} - (i\alpha) U_B \hat{v}_{1,1}].$$

REFERENCES

- 1A. Fedorov, "Transition and stability of high-speed boundary layers," *Annu. Rev. Fluid Mech.* **43**, 79-95 (2011).
- 2X. Zhong and X. Wang, "Direct numerical simulation on the receptivity, instability, and transition of hypersonic boundary layers," *Annu. Rev. Fluid Mech.* **44**, 527-561 (2012).
- 3Y. S. Kachanov, "Physical mechanisms of laminar-boundary-layer transition," *Annu. Rev. Fluid Mech.* **26**, 411-482 (1994).
- 4L. M. Mack, "Review of linear compressible stability theory," in *Stability of Time Dependent and Spatially Varying Flows*, edited by D. L. Dwoyer and M. Y. Hussaini (Springer, New York, 1987), pp. 164-187.
- 5F. T. Smith, "On the first-mode instability in subsonic, supersonic or hypersonic boundary layers," *J. Fluid Mech.* **198**, 127-153 (1989).
- 6Y. Liu, M. Dong, and X. Wu, "Generation of first Mack modes in supersonic boundary layers by slow acoustic waves interacting with streamwise isolated wall roughness," *J. Fluid Mech.* **888**, A10 (2020).
- 7F. T. Smith and S. N. Brown, "The inviscid instability of a blasius boundary layer at large values of the Mach number," *J. Fluid Mech.* **219**, 499-518 (1990).
- 8S. Cowley and P. Hall, "On the instability of hypersonic flow past a wedge," *J. Fluid Mech.* **214**, 17-42 (1990).
- 9M. Dong, Y. Liu, and X. Wu, "Receptivity of inviscid modes in supersonic boundary layers due to scattering of free-stream sound by localised wall roughness," *J. Fluid Mech.* **896**, A23 (2020).
- 10A. Thumm, "Numerische untersuchungen zum laminar-turbulenten strömungsumschlag in transsonischen grenzschichtströmungen," Ph.D. thesis (Universität Stuttgart, 1991).
- 11H. Fasel, A. Thumm, and H. Bestek, "Direct numerical simulation of transition in supersonic boundary layers: Oblique breakdown," in *Transitional and Turbulent Compressible Flows* (ASME, 1993), pp. 77-92.

- ¹²C. Chang and M. R. Malik, "Oblique-mode breakdown and secondary instability in supersonic boundary layers," *J. Fluid Mech.* **273**, 323–360 (1994).
- ¹³S. J. Leib and S. S. Lee, "Nonlinear evolution of a pair of oblique instability waves in a supersonic boundary layer," *J. Fluid Mech.* **282**, 339–371 (1995).
- ¹⁴C. S. J. Mayer, S. Wernz, and H. F. Fasel, "Numerical investigation of the nonlinear transition regime in a Mach 2 boundary layer," *J. Fluid Mech.* **668**, 113–149 (2011).
- ¹⁵C. S. J. Mayer, D. A. Von Terzi, and H. F. Fasel, "Direct numerical simulation of complete transition to turbulence via oblique breakdown at Mach 3," *J. Fluid Mech.* **674**, 5–42 (2011).
- ¹⁶J. Sivasubramanian and H. F. Fasel, "Direct numerical simulation of transition in a sharp cone boundary layer at Mach 6: Fundamental breakdown," *J. Fluid Mech.* **768**, 175–218 (2015).
- ¹⁷C. Hader and H. F. Fasel, "Direct numerical simulations of hypersonic boundary-layer transition for a flared cone: Fundamental breakdown," *J. Fluid Mech.* **869**, 341–384 (2019).
- ¹⁸L. Ng and G. Erlebacher, "Secondary instabilities in compressible boundary layers," *Phys. Fluids* **4**, 710–726 (1992).
- ¹⁹Y. G. Ermolaev, A. D. Kosinov, and N. V. Semionov, "Experimental investigation of laminar-turbulent transition process in supersonic boundary layer using controlled disturbances," in *IUTAM Symposium on Nonlinear Instability and Transition in Three-Dimensional Boundary Layers*, edited by P. W. Duck and P. Hall (Springer, Dordrecht, Netherlands, 1996), pp. 17–26.
- ²⁰C. S. J. Mayer, H. F. Fasel, M. Choudhari, and C. Chang, "Transition onset predictions for oblique breakdown in a Mach 3 boundary layer," *AIAA J.* **52**, 882–886 (2014).
- ²¹X. Y. Jiang, C. B. Lee, X. Chen, C. R. Smith, and P. F. Linden, "Structure evolution at early stage of boundary-layer transition: Simulation and experiment," *J. Fluid Mech.* **890**, A11 (2020).
- ²²K. J. Franko and S. K. Lele, "Breakdown mechanisms and heat transfer overshoot in hypersonic zero pressure gradient boundary layers," *J. Fluid Mech.* **730**, 491–532 (2013).
- ²³A. Novikov, I. Egorov, and A. Fedorov, "Direct numerical simulation of wave packets in hypersonic compression-corner flow," *AIAA J.* **54**, 2034–2050 (2016).
- ²⁴M. E. Goldstein and S. W. Choi, "Nonlinear evolution of interacting oblique waves on two-dimensional shear layers," *J. Fluid Mech.* **207**, 97–120 (1989).
- ²⁵X. Wu, S. Lee, and S. J. Cowley, "On the weakly nonlinear three-dimensional instability of shear layers to pairs of oblique waves: The Stokes layer as a paradigm," *J. Fluid Mech.* **253**, 681–721 (1993).
- ²⁶W. Mangler, "Zusammenhang zwischen ebenen und rotations symmetrischen grenzschichten in kompressiblen flüssigkeiten," *Z. Angew. Math. Mech.* **28**, 97–103 (1948).
- ²⁷X. Wu and M. Dong, "A local scattering theory for the effects of isolated roughness on boundary-layer instability and transition: Transmission coefficient as an eigenvalue," *J. Fluid Mech.* **794**, 68–108 (2016).
- ²⁸M. Dong and L. Zhao, "An asymptotic theory of the roughness impact on inviscid Mack modes in supersonic/hypersonic boundary layers," *J. Fluid Mech.* **913**, A22 (2021).
- ²⁹M. R. Malik, "Numerical methods for hypersonic boundary layer stability," *J. Comput. Phys.* **86**, 376–413 (1990).
- ³⁰F. P. Bertolotti, T. Herbert, and P. R. Spalart, "Linear and nonlinear stability of the Blasius boundary layer," *J. Fluid Mech.* **242**, 441–474 (1992).
- ³¹L. Zhao, C. Zhang, J. Liu, and J. Luo, "Improved algorithm for solving nonlinear parabolized stability equations," *Chin. Phys. B* **25**, 084701 (2016).
- ³²L. Brandt, P. Schlatter, and D. S. Henningson, "Transition in boundary layers subject to free-stream turbulence," *J. Fluid Mech.* **517**, 167–198 (2004).
- ³³P. Durbin and X. Wu, "Transition beneath vortical disturbances," *Annu. Rev. Fluid Mech.* **39**, 107–128 (2007).
- ³⁴A. Zhang, M. Dong, and Y. Zhang, "Receptivity of secondary instability modes in streaky boundary layers," *Phys. Fluids* **30**, 114102 (2018).
- ³⁵Y. Zhang, W. Zhou, and X. Chen, "An investigation on the disturbance evolution and the transition by resonant-triad interactions with a side-frequency disturbance in a boundary layer," *Phys. Fluids* **32**, 074101 (2020).